

Analysis of power-law exponents by maximum-likelihood maps

Jordi Baró* and Eduard Vives†

*Departament d'Estructura i Constituents de la Matèria, Facultat de Física, Universitat de Barcelona,
Diagonal 647, E-08028 Barcelona, Catalonia, Spain*

(Received 8 February 2012; published 19 June 2012)

Maximum-likelihood exponent maps have been studied as a technique to increase the understanding and improve the fit of power-law exponents to experimental and numerical simulation data, especially when they exhibit both upper and lower cutoffs. The use of the technique is tested by analyzing seismological data, acoustic emission data, and avalanches in numerical simulations of the three-dimensional random field Ising model. In the different examples we discuss the nature of the deviations observed in the exponent maps and some relevant conclusions are drawn for the physics behind each phenomenon.

DOI: [10.1103/PhysRevE.85.066121](https://doi.org/10.1103/PhysRevE.85.066121)

PACS number(s): 89.75.Da, 64.60.av, 91.30.-f, 81.30.Kf

I. INTRODUCTION

For the last few decades the study of critical phenomena has received a great deal of attention in many different areas of physics [1]. Criticality is often identified by the presence of statistical scale-free distributions of different magnitudes when a system evolves in time or when it is driven by an external force. The physical nature of the measured response can be very different: energy, displacement, magnetization, volume, polarization, resistivity, etc. In all cases, when the sudden changes (often called avalanches) of such magnitudes exhibit a statistical distribution compatible with a power-law probability density function $g(x) dx \sim x^{-\alpha} dx$ one gains confidence about the existence of criticality. In some cases criticality has also been referred to as “crackling noise” [2]. At criticality the response of the system is characterized solely by the critical exponents α . The theoretical understanding provided by the use of renormalization group techniques [3] states, in many cases, that critical exponents show a certain degree of universality. Thus, it has become extremely important to determine the values of α to a high degree of accuracy and confidence.

Within this framework, it is important to develop tools to test the power-law behavior of data samples and to fit critical exponents. The development of these statistical tools cannot be done without taking into account the limitations inherent to data acquisition. Typically in physics, data come from experiment or computer simulation and in both cases one has boundaries to the proposed scale-free behavior. These boundaries are not necessarily sharp or well defined. In experiments one finds unavoidable noise deforming the power-law distribution in the small-event region and different kinds of instrument saturation in the large-event region. One should take into account the fact that it is difficult to find instruments (amplifiers, voltmeters, etc.) that allow measurements with a range of more than five decades. In simulations one also finds unavoidable limitations: for instance, one has a minimum lattice parameter or particle size that alters the small-event distribution and finite-size effects deforming the large events. Since simulations with more than 10^5 particles are scarce,

it is also difficult to find power-law distributions extending many decades in numerical works. In addition, the existence of deformations in the region of small events is understood not only because of the reasons discussed above with a physical origin but also because of a mathematical constraint: a pure power-law probability density with $\alpha > 1$ cannot be normalized without a theoretical lower limit x_{\min} .

It is easy to understand that a naked-eye analysis of standard histograms can be easily fooled, not only by the lack of statistics (insufficient data in the recorded sample) but also by the anomalies in the large- and small-event regions. The same may happen with traditional fitting methods such as the least-squares method (both linear and nonlinear), which, for instance, depends on the binning process that is performed in order to plot the histograms.

Many years ago most of the community adopted the maximum-likelihood (ML) estimation method [4–6] as the safest way to treat data, although it is still frequent to see papers using alternative, error-prone fitting methods. Within this scenario, the work done by Newman and co-workers should be pointed out [6]. Using ML methods they have nicely illustrated how to test the power-law character of data and how to obtain good estimations (and error bars) of critical exponents. One of the proposed techniques consists of studying how robust the ML exponent is when the analyzed data are restricted to being higher than an imposed lower cutoff X_{low} that is varied by several decades. By this method one studies the deformation of the fitted exponent due to undesired effects in the region of small events.

In this paper we will study the extension of this technique to the analysis of the ML exponent as a function of both an imposed lower cutoff X_{low} and an imposed higher cutoff X_{high} . This will render so-called ML exponent maps [7]. Using this method we expect to be able to improve exponent estimation in the case in which experimental or simulation data present distortions not only in the region of small events but also in the large-event region.

In Sec. II we will revisit the ML method and define ML exponent maps. We will include a discussion on numerical methods, evaluation of error bars, and analysis of synthetic data obtained by pseudo-random-number generation. In Sec. III we will apply the proposed analysis technique to the study of three seismological catalogs from Japan, the San Andreas fault, and the very recent activity on the island of

*jordibaro@ecm.ub.es

†eduard@ecm.ub.es

El Hierro (Canary Islands). In Sec. IV we will study three experimental cases corresponding to the measurement of the energy of acoustic emission events in different phenomena in solids, from previous literature. The three sets of experiments have been carried out with the same experimental setup but with different experimental constraints (noise, amplification, etc.). The three cases correspond to (i) the compression of a porous material (Vycor) [8], (ii) a cubic-tetragonal structural transition in FePd [9], and (iii) a cubic-monoclinic structural transition in a CuZnAl shape memory alloy [10]. In Sec. V we will illustrate how to apply the technique to the study of numerical simulations of the three-dimensional (3D) random field Ising model with metastable dynamics, which is one of the prototypical frameworks for avalanche criticality [11,12]. Finally, in Sec. VI we will supply a summary and draw conclusions.

II. MAXIMUM-LIKELIHOOD EXPONENT MAP

Let us consider a sample of measurements $\{X_i\}$ ($i = 1, \dots, N$) that we assume to be statistically independent. We will denote by capital letters X_{\max} and X_{\min} the smallest and the largest values in the sample set. Our aim is to model this set with a power-law probability density:

$$g(x) dx = \frac{x^{-\gamma}}{\zeta(\gamma)} dx, \quad x_{\min} < x < x_{\max}, \quad (1)$$

where γ is the exponent that we wish to estimate and $\zeta(\gamma)$ denotes a normalization function. This normalization function will depend on γ and the theoretical upper (x_{\max}) and lower (x_{\min}) bounds, as will be discussed below. (The case $x_{\max} \rightarrow \infty$ is a particular case of our analysis). Note that these theoretical limits will not necessarily coincide with the maximum X_{\max} and minimum X_{\min} values in the sample. Nevertheless, given the power-law character of the probability density we expect that X_{\min} will be much closer to x_{\min} than X_{\max} to x_{\max} . Table I clarifies the generic definitions of the limits and cutoffs that will be used within this section. The likelihood function \mathcal{L} is defined as the probability that the set of measurements $\{X_i\}$ can be obtained by the proposed model:

$$\mathcal{L}(\gamma) = \prod_{i=1}^N g(X_i). \quad (2)$$

The maximum likelihood estimation method consists of choosing the value of γ that maximizes the likelihood function, i.e., the value that makes the sample that we have obtained the most likely one to have occurred.

In order to evaluate the deviations of data with respect to the proposed model, in this work we will perform ML estimations by restricting the original data within the imposed lower cutoff

TABLE I. Terminology used in this work to define the generic bounds and cutoffs used for the theoretical analysis in this section

Symbols	Meaning
x_{\min}, x_{\max}	sharp bounds of the density $g(x)$
X_{\min}, X_{\max}	extreme values in the sample $\{X_i\}$
$X_{\text{low}}, X_{\text{high}}$	cutoffs imposed on the sample for the analysis

X_{low} and the imposed higher cutoff X_{high} , different from the theoretical limits x_{\min} and x_{\max} , which are generally unknown. We will use the symbol $\hat{\gamma}$ to distinguish the exponent estimated within a restricted interval from the exponent estimated from the whole available sample. We will use n ($n < N$) to denote the number of data points of the restricted set. The normalization factor of the probability density with imposed cutoffs is

$$\zeta(\hat{\gamma}) = \int_{X_{\text{low}}}^{X_{\text{high}}} x^{-\hat{\gamma}} dx = \frac{X_{\text{low}}^{1-\hat{\gamma}} - X_{\text{high}}^{1-\hat{\gamma}}}{\hat{\gamma} - 1}. \quad (3)$$

The best estimation of $\hat{\gamma}$ is consequently found by maximizing the likelihood function:

$$0 = \frac{\partial \ln \mathcal{L}(\hat{\gamma})}{\partial \hat{\gamma}} = - \sum_{\{X_{\text{low}} < X_i < X_{\text{high}}\}} \ln(X_i) - n \frac{\zeta'(\hat{\gamma})}{\zeta(\hat{\gamma})}, \quad (4)$$

where

$$\frac{\zeta'(\hat{\gamma})}{\zeta(\hat{\gamma})} = \frac{1}{1-\hat{\gamma}} - \frac{X_{\text{high}}^{1-\hat{\gamma}} \ln X_{\text{high}} - X_{\text{low}}^{1-\hat{\gamma}} \ln X_{\text{low}}}{X_{\text{high}}^{1-\hat{\gamma}} - X_{\text{low}}^{1-\hat{\gamma}}}. \quad (5)$$

We should mention that for the case in which the data are discrete (for instance, in many simulations of lattice models) the above treatment should be slightly modified. In this case, the data consist of the frequencies of occurrence $f(k)$ of a discrete set of values $\{k\}$ (which we will assume to be integers). We would like to fit it with a power-law probability function (called a Zeta or Zipf function) [4]:

$$p(k) = \frac{k^{-\gamma}}{\zeta(\gamma)}, \quad k_{\min} \leq k \leq k_{\max}. \quad (6)$$

By following the same procedure as above, when we restrict ourselves to data within imposed cutoffs K_{low} and K_{high} , the normalization function is

$$\zeta(\hat{\gamma}) = \sum_{k=K_{\text{low}}}^{K_{\text{high}}} k^{-\hat{\gamma}} \quad (7)$$

and the derivative of the likelihood function will read

$$\frac{\partial \ln \mathcal{L}}{\partial \hat{\gamma}} = - \sum_{k=K_{\text{low}}}^{K_{\text{high}}} f(k) \ln(k) + N \frac{\sum_{K_{\text{low}}}^{K_{\text{high}}} k^{-\hat{\gamma}} \ln(k)}{\sum_{K_{\text{low}}}^{K_{\text{high}}} k^{-\hat{\gamma}}}. \quad (8)$$

As opposed to what happens in the case in which one considers only a lower cutoff, Eqs. (5) and (8) cannot be solved analytically. Thus, in this work, we will use the false position method in order to find roots [13]. This method generates a sequence of recursively smaller intervals that always include the root of the equation. The monotonicity of the derivative of $\ln \mathcal{L}$ [14] ensures that the false position method always converges to the root. We have chosen arbitrary starting values of $\hat{\gamma}_1 = 1$ and $\hat{\gamma}_2 = 3.5$, and we have iterated the algorithm M times until an interval $(\hat{\gamma}_{M-1}, \hat{\gamma}_M)$ is reached with a distance smaller than 0.005.

By changing the X_{low} and X_{high} cutoffs we can plot the values of the ML estimations of $\hat{\gamma}$ using a color scale and thus obtain the exponent map. Examples are shown in Fig. 1 and throughout the paper. Contour lines (in white) will also be shown separating exponent values in steps of 0.1. The maps exhibit a triangular shape since they are obviously limited by

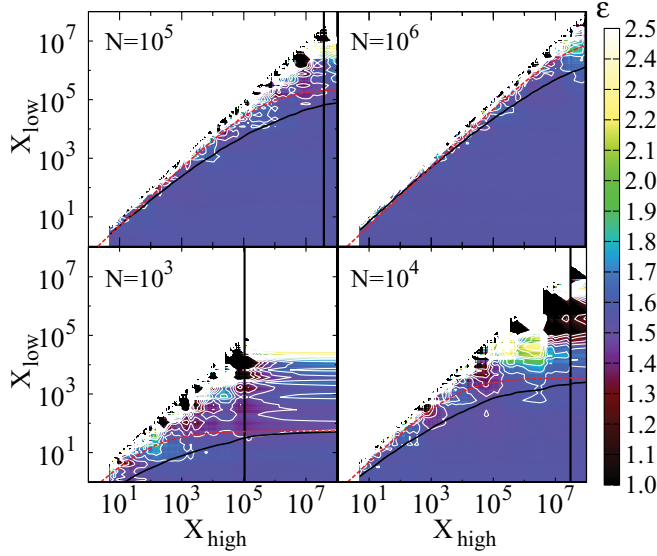


FIG. 1. (Color online) Exponent maps obtained from synthetic data. The data sets correspond to a theoretical probability density function with exponent $\gamma = 1.55$ and bounds $x_{\min} = 1$ and $x_{\max} = 10^8$. The label N indicates the size of the sample set. The two curved lines indicate the limits above which the standard deviation becomes greater than 0.05: The red dashed curved line (above) corresponds to the estimation using Eq. (11) and the black continuous curved line (below) to Eq. (10). The vertical straight line marks the highest value in the sample X_{\max} .

the condition $X_{\text{high}} > X_{\text{low}}$. The main goal of the map is to check the existence of a flat plateau (with a homogeneous color which is free of contour lines) in which the exponent is independent of the cutoffs and thus confirm the scale-free behavior of the data. The map also allows anomalies to be identified that can have different origins, as will be discussed in the following sections by the use of examples.

One of the advantages of using the false position method for root finding is that we straightforwardly obtain an estimation of the second derivative of $\ln \mathcal{L}$ at the maximum:

$$\left. \frac{\partial^2 \ln \mathcal{L}}{\partial \hat{\gamma}^2} \right|_{\text{max}} \sim \frac{\left. \frac{\partial \ln \mathcal{L}}{\partial \hat{\gamma}} \right|_M - \left. \frac{\partial \ln \mathcal{L}}{\partial \hat{\gamma}} \right|_{M-1}}{\hat{\gamma}_M - \hat{\gamma}_{M-1}}. \quad (9)$$

By assuming Gaussian behavior of the likelihood function (which is ensured by the central limit theorem when n is large enough) and under very general conditions [15], the second derivative provides us with an approximation to the standard deviation of the estimated exponent,

$$\sigma_{\hat{\gamma}} = \left[- \left. \frac{\partial^2 \ln \mathcal{L}}{\partial \hat{\gamma}^2} \right|_{\text{max}} \right]^{-1/2}. \quad (10)$$

It is easy to check that this expression, when $x_{\max} \rightarrow \infty$, reduces to the equation proposed in Ref. [6]:

$$\sigma_{\hat{\gamma}} = \frac{\hat{\gamma} - 1}{\sqrt{n}}. \quad (11)$$

As a first test of the usefulness of the ML exponent maps, we studied synthetic data [6] generated according to a power-law

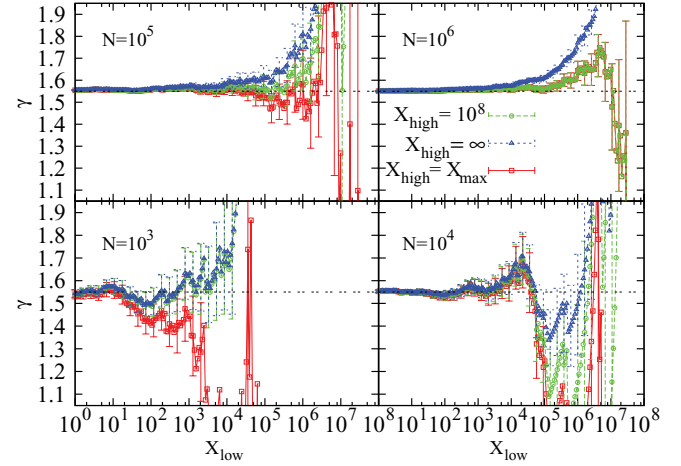


FIG. 2. (Color online) Comparison of the behavior of the exponent fitted to synthetic data as a function of the lower cutoff X_{low} when X_{high} is fixed. Squares (red) correspond to $X_{\text{high}} = x_{\max} = 10^8$ (the theoretical limit of the synthetic data), circles (green) to $X_{\text{high}} = X_{\max}$ (the maximum value found in the sample), and triangles (blue) to $X_{\text{high}} = \infty$.

probability density with theoretical limits $x_{\min} \leq x < x_{\max}$:

$$g(x) dx = (\gamma - 1) \frac{x^{-\gamma}}{x_{\min}^{1-\gamma} - x_{\max}^{1-\gamma}} dx, \quad (12)$$

with $\gamma = 1.55$, $x_{\min} = 1$, and $x_{\max} = 10^8$. The synthetic data samples were obtained using the RANECU generator [16] for uniform random numbers in the $[0, 1)$ interval and transformed using the method based on the inverse cumulative distribution function $F^{-1}(z)$. For the proposed probability density (12) the transformation function that converts uniform random numbers z into the desired ones is given by

$$x = F^{-1}(z) = \left[x_{\max}^{1-\gamma} - z(x_{\max}^{1-\gamma} - x_{\min}^{1-\gamma}) \right]^{1/(1-\gamma)}. \quad (13)$$

Figure 1 shows the resulting maps corresponding to four samples of increasing size N as indicated by the legends. The first observation is that the size N of the sample is crucial in order to obtain a clean plateau corresponding to the correct exponent. Only when $N \gtrsim 10^4$ does the plateau extend for several “square” decades.

We have indicated the position of the maximum value X_{\max} obtained in the sample by a vertical black line. The variations of the fitted exponent observed from this line to the right are simply a consequence of changing the imposed upper cutoff X_{high} in a region without available data due to the lack of statistics. This lack of data between X_{\max} and X_{high} is relevant for the fitting method and, *a priori*, should be taken into account. Furthermore, the imposed cutoff X_{high} can be moved above the theoretical limit x_{\max} or set to be ∞ . This will then be equivalent to fitting the synthetic data (generated with a theoretical upper limit) with a model without such a limit. In the maps in Fig. 1 we have kept the imposed cutoff X_{high} below the theoretical cutoff x_{\max} , but note that for real data (e.g., in the following examples) this theoretical cutoff will be unknown.

Figure 2 shows the behavior of the fitted exponent $\hat{\gamma}$ as a function of the lower cutoff X_{low} for the same synthetic data

samples as in Fig. 1. We have compared three different ML estimations corresponding to three choices of X_{high} :

(1) Green circles correspond to the ML estimation of the exponent obtained by fixing $X_{\text{high}} = x_{\text{max}} = 10^8$, the theoretical upper limit. This is nothing more than the profile of the ML exponent map along the vertical right border at 10^8 in Fig. 1. This would be the correct way to perform the ML estimation if one could have *a priori* knowledge of the true upper cutoff.

(2) Blue triangles (higher symbols) correspond to the ML estimation obtained by neglecting the existence of an upper limit in the power-law distribution, i.e., fixing $X_{\text{high}} = \infty$. This would precisely correspond to the method proposed by Ref. [6].

(3) Red squares (lower symbols) correspond to the ML estimation obtained by fixing the higher cutoff of the data to the maximum value found in the sample $X_{\text{high}} = X_{\text{max}}$. It corresponds to the profile of the map along the vertical black lines in Fig. 1.

For small N Method 3 underestimates the exponent because it neglects the fact that no data have been observed between X_{max} and x_{max} . However, for $N \gtrsim 10^4$, one can see that Method 3 renders exponents that are very similar to the correct ones (Method 1). For $N = 10^6$ Method 3 is clearly better than Method 2, which neglects the existence of an upper boundary to the distribution: it can be seen that the two coinciding estimation methods (red squares and green circles) exhibit a larger plateau (by more than one decade) than the blue triangles.

It is also interesting to discuss the strong fluctuations of the ML exponent close to the diagonal of the maps, which can be observed in Fig. 1. These are due to the small size n of the restricted sample set that increases the statistical fluctuations. We can locate the region where the standard deviation of the ML estimate is lower than ± 0.05 [17] by using the formulas (10) or (11). These low-error regions correspond to the areas below the continuous (black) and dashed (red) curved lines, respectively. As can be seen, both estimations of the error differ, even in the region of small events. The estimation that takes into account the existence of both a low and a high cutoff obtained from Eq. (10) gives a better separation between the regions with meandering contour levels and the smooth, flat plateau.

To conclude this section, let us summarize what we have learned from the analysis of synthetic data: it does not make much sense to increase the higher cutoff X_{high} above the maximum value in the data sample X_{max} unless we have independent information of the theoretical limit x_{max} . Therefore, in the maps presented in the following sections we will scan the higher and lower cutoffs only within X_{min} and X_{max} . Thus, the vertical right border of the maps will coincide with the vertical black line plotted in Fig. 1. In addition, we will use the error estimation proposed by Eq. (10) and plot, on the maps, the curved line separating the region with error bars greater than ± 0.05 (above the line) from the region with lower error bars (below).

III. SEISMOLOGICAL CATALOG ANALYSIS

The Gutenberg-Richter law [18,19] describing the statistical distribution of earthquake magnitudes is one of the most famous examples of a scale-free phenomenon already discussed using ML methods in previous works [20].

Theoretical studies have proposed different physical models (e.g., Burridge-Knopoff [21], Olami-Feder-Christensen [22], and damage rheology [23]) and framework theories such as the so-called self-organized criticality [24–26] have explained, to a certain extent, the reasons behind this critical behavior. It is not our purpose to gain any understanding of seismology, but only to use some of the available earthquake catalogs in order to test the behavior of ML exponent maps.

Earthquakes are historically characterized by a quantity called magnitude M , which aims to be a logarithmic measure of the “size” or “energy released” during the earthquake. The Gutenberg-Richter law [18] refers to the number of earthquakes $N_{>}(M)$ with a magnitude larger than a certain value M . As a function of magnitude, the Gutenberg-Richter law can be written as

$$N_{>}(M) \propto -bM, \quad (14)$$

with $b \sim 1.0$. The measurement of earthquake magnitudes and energies is still a challenging issue for seismology. As the medium is too large to collect a significant amount of radiated energy, seismologists must rely on measurements of the sparse network of seismic stations in order to locate and estimate the “size” of an earthquake. Because of this, many different criteria are used, depending on the region, earthquake energy range, available instruments, etc. The catalogs usually contain mixed data corresponding to different definitions of the magnitude M . These definitions are not fully equivalent, especially for small earthquakes [19,27]. There are also different definitions of the “energy” associated with an earthquake (all of them being approximately linearly related): seismic moment, strain energy drop, radiated energy, etc. In this work we will use a broadly accepted formula [28] that allows an approximate conversion of the different “magnitudes” M to the minimum strain energy drop E as

$$\log_{10} E = 1.5M + 4.8, \quad (15)$$

where E is the energy in joules. Using the Gutenberg-Richter law (14) and Eq. (15), one can write the probability density for earthquakes with energies between E and $E + dE$ as

$$p(E) dE \sim E^{-\epsilon} dE, \quad (16)$$

where $\epsilon = 1 + (b/1.5) \simeq 1.67$ is the expected exponent characterizing the power-law distribution of earthquake energies.

We have computed the ML exponent maps corresponding to three earthquake catalogs:

(1) The subduction process taking place in the Japan Trench makes it one of the most active seismological regions in the world. The area is quite well documented because of the vicinity of the Japanese islands. We studied the exponent map corresponding to the energy distribution for all the seismological events registered as earthquakes in the ANSS [29] catalog from 1 January 2000, 00:00:00 to 9 November 2011, 17:32:36 within the region enclosed between latitudes 28°N and 48°N and longitudes 128°E and 148°E . The registered data correspond to the $N = 14\,509$ events above $M = 2.7$, where the the Tōhoku earthquake of 11 March 2011 was the most serious event with an estimated magnitude of $M = 9.0$.

(2) San Andreas fault system [30], beneath the region occupied by the states of California and Nevada, is probably the most frequently monitored seismic region in the world

and the best documented in catalogs. We will therefore take it as a precise example of a seismological strike-slip process. The data analyzed here correspond to the seismic signals registered as earthquakes in the ANSS [29] catalog with its epicenter within the area of latitudes between 30°N and 42°N and longitudes between 114°W and 126°W during the period between 1 January 2000, 00:00:00 and 9 November 2011, 17:43:00. In order to avoid the presence of a possible noise background, we selected only those earthquakes with a magnitude greater than $M = 0.4$. The strongest earthquake was recorded on 15 June 2005 off the coast of Northern California with a magnitude of $M = 7.2$. The data set has $N = 453\,372$ events.

(3) As a completely different seismological phenomenon (very localized in space and time), we considered the recent submarine volcanic eruption of La Restinga off the island of El Hierro (Canary Islands), which started in the summer of 2011. The volcanic activity triggered an earthquake swarm [31] which is expected to have quite different behavior from typical tectonic processes. We considered the data obtained from the IGN [32] catalog from 8 June 2011, 00:52:00 until 7 February 2012, 12:00:00 in the region enclosed by latitudes from 26.8°N to 27.6°N and longitudes from 17.85°W to 18.2°W . The data set has $N = 12\,158$ events

The three ML exponent maps are shown in Fig. 3. We have kept the same scales in order to clearly reveal the different size N of the statistical samples. Figure 4 shows the behavior of the fitted exponent ϵ as a function of the lower cutoff E_{low} when the higher cutoff E_{high} is fixed to the maximum value in the sample set, i.e., the profile of the map along the vertical right borders in Fig. 3.

The first observation is that there is an almost perfect plateau exhibited by the San Andreas data (middle diagram) for a value close to the expected theoretical value $\epsilon = 1.67$. Despite some deformation, indications of a plateau are also observed for the other two sets, Japan (top diagram) and El Hierro (bottom diagram). For the El Hierro data the coincidence is remarkable, given the different physical origins of the earthquake sequence.

A second important observation is the deformation of the plateau (toward low exponent values) for the Japan data in the region of $E_{\text{low}} < 10^{10}\text{J}$. A plausible explanation for this deformation is that the statistics for small earthquakes in the Japan catalog is incomplete. The same tendency can be observed for the San Andreas data, but for much lower minimum cutoffs, $E_{\text{low}} < 10^8\text{J}$, almost coinciding with the lower border of the map in Fig. 3 (middle diagram). The oscillation of the fitted exponent for the Japan data that can be seen on the maps (as contour lines with a parabolic horizontal shape starting from the right border) is surprising as well as the existence of a maximum (about $E_{\text{low}} \sim 10^{11}\text{--}10^{12}\text{J}$) on the profile shown in Fig. 4. We are unable to provide an explanation for this behavior, but it could be caused by the different methods used to estimate magnitudes and/or energies depending on the earthquake magnitude range.

IV. ACOUSTIC EMISSION DATA ANALYSIS

As a second set of experimental examples, we have focused on much smaller energy scales. Different processes, which have been classified as critical or crackling noise, take place in

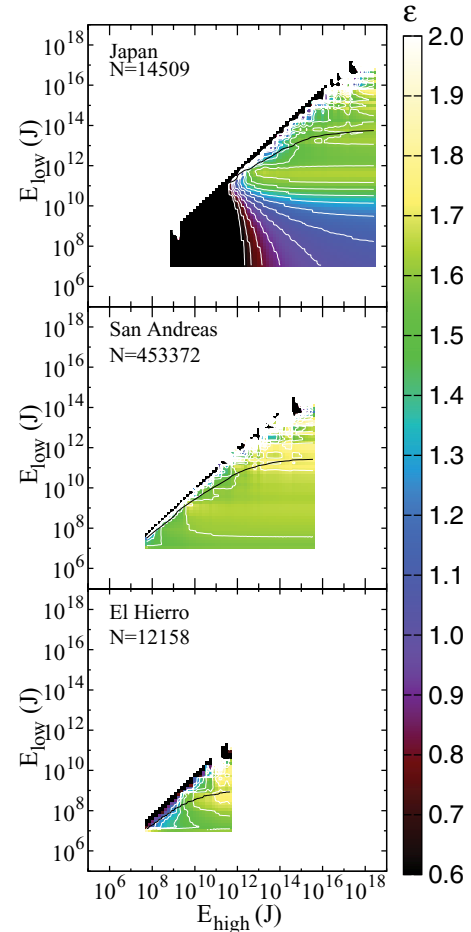


FIG. 3. (Color online) ML exponent map corresponding to the earthquake data from Japan, the San Andreas fault, and El Hierro. White contour lines are separated by 0.1 units. The region above the black line corresponds to estimated statistical error bars greater than ± 0.05 .

solids, exhibiting a certain degree of disorder when driven by an external force or by a temperature ramp. Examples include superconductivity [33], capillary condensation [34], acoustic emission in structural transitions [35–37], Barkhausen

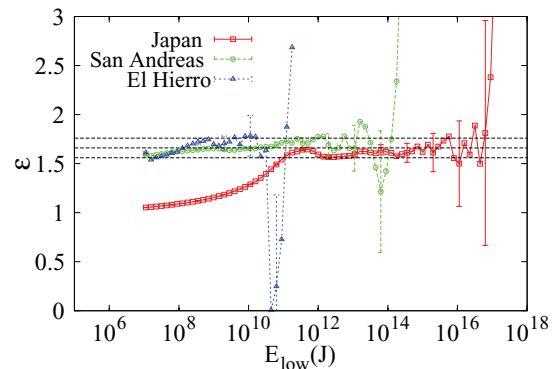


FIG. 4. (Color online) Behavior of the ML exponent as a function of the lower cutoff E_{low} for a fixed higher cutoff equal to the maximum value in the sample set. Only a few error bars are indicated. The horizontal dashed lines show the theoretically expected value of 1.66 and an error bar of ± 0.10 .

noise in magnetism [38,39], and fracture [40]. In many cases, theoretical studies have provided general frameworks to understand the origin of this criticality [2,41–45].

The following three experimental examples correspond to data recorded using the acoustic emission (AE) technique [46]. Propagation of cracks or the sudden movement of internal interfaces generate acoustic waves in the ultrasonic range that propagate through the solid and that can be recorded by appropriate transducers on the surface. The AE method is equivalent to the method used to monitor earthquakes, but on a much smaller scale. It is interesting to describe here some details in order to understand the deviations that will be observed in the maps.

The most common piezoelectric transducers, coupled to the sample surface, generate a voltage signal $V(t)$ proportional to the speed of the incident elastic wave that is amplified. Using a predefined threshold (above the unavoidable experimental electrical and mechanical noise), it is possible to define individual AE events [47]. The beginning of an event occurs at a time t_1 when the voltage exceeds the threshold. The end of the event occurs when the signal falls below the threshold at t_2 and remains below the threshold for more than a certain predefined time called the hit definition time (HDT), typically in the range of 10–100 μ s. The fast integration of the $V^2(t)$ signal from t_1 to t_2 , normalized by a reference resistance, renders an estimation of the energy recorded by the transducer, which is assumed to be proportional to the energy released by the physical process generating the elastic wave.

It is worth mentioning some experimental limitations of most standard setups: (i) Acquisition systems, due to limited memory, have an internal maximum limit on the duration of a signal as well as a maximum limit on the voltage that saturates the amplifier. In the case that such maxima are exceeded, the signal is truncated both in voltage and/or duration. This represents a deformation in the large-event region and a not totally sharp cutoff in the measured energy since both voltage and duration can be independently exceeded. (ii) A second experimental problem that needs to be considered is due to the attenuation of ultrasound inside the material and the distance from the source of the AE event to the transducer. If the studied samples are small (compared to typical length scales for exponential attenuation or compared to typical transducer sizes) we expect that data recorded by a single transducer would not be very distorted by the distance to the source. However, if samples become large, the quality of the overall power-law distribution becomes poorer. One could then use several transducers to locate the position of the source of the event and correct for attenuation. This has been achieved in some cases [48,49], though, in general, it is a complicated procedure. The examples below correspond to the use of a single transducer. (iii) A third problem is that counting of the small signals is lower than expected for different reasons: an important fraction of signals that happen to be very short in time and/or amplitude cannot be detected by the acquisition setup (because they are too short for the sampling frequency or the amplitude is below the threshold value), or some of the small signals may be overlapped by the tails of previous signals due to dead-time HDT.

In the cases analyzed in the following three sections, the same experimental setup for the acquisition of AE has

been used: a PCI2 system from the MISTRAS Group, which consists of an 18-bit A/D converter working at a base sampling rate of 40 MHz. The transducers are also the same in the three examples (micro80). This makes the ML exponent maps easy to compare. The amplification factor, the threshold, and the number of recorded signals used in each case are different, given the different noise conditions and differing nature of the studied phenomenon and driving force. Although the acquisition card is only 18 bits (~ 5 decades), the measured energies by the fast integration algorithm may theoretically extend many more decades. In order to compare the different studies, we will keep the same scales: from 10^{-17} to 10^{-9} J for energy and from 1.0 to 2.5 for the fitted exponent ϵ .

A. Mesoporous SiO₂ under compression

The study of noise in porous materials under compression is important for the prediction of accidents in mining. In this first example [8] two samples of a porous material SiO₂ (Vycor) with two parallel faces are compressed between two plates with a lineally increasing load in time. The AE sensor is attached to one of the plates. There are two sets of data studied corresponding to the AE events recorded at two loading rates: 0.2 and 1.6 kPa/s. The study of the influence of the driving rate is important because, in some cases, it affects the fitted exponents due to the overlap of large and small avalanches [50,51]. The material cracks under compression and the recorded AE signals show a power-law distribution of energies. In this case a preamplifier of 60 dB was used and the threshold was selected to be 26 dB. The number of recorded signals was $N = 11\,022$ and $N = 28\,652$ for the first and second set, respectively.

Figure 5 shows the ML exponent maps obtained with the two driving rates. It is clear that, in both cases, there is a vast region of the map with a constant plateau corresponding to a common value of the exponent close to 1.4. This means that the exponent is robust against changes in the cutoffs by several decades. The small colored spots observed close to the diagonal of the map as well as the large peak in the upper right-hand corner correspond to expected statistical fluctuations, above the black line indicating when the statistical error bar becomes larger than ± 0.05 . The black region in the bottom left-hand corner corresponds to the fact that the exponent decreases when only an important fraction of very low signals is included in the analysis, which gives an erroneous estimation for the reasons explained above. Basically, no other deviations are observed in this example.

Figure 6 shows the analysis of the profiles of the map along the right vertical border ($E_{\text{high}} = E_{\text{max}}$) compared to the analysis proposed in Ref. [6] by assuming no upper limit for the power-law distribution ($E_{\text{high}} = \infty$). As can be observed, the two profiles are similar but are not identical. They show a clean plateau at 1.39 ± 0.02 for three decades (10^{-15} – 10^{-12}). The profile obtained by fixing the highest cutoff to the maximum value in the sample (i.e., along the right-hand border of the ML exponent map in Fig. 5) shows flatter behavior along, at least, one more decade.

Therefore, one can conclude that this example shows a very robust power-law behavior, comparable to that observed for seismological data.

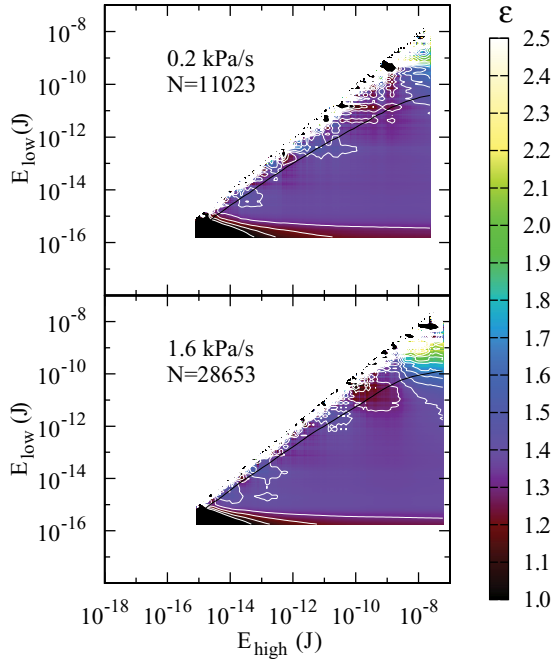


FIG. 5. (Color online) ML exponent maps corresponding to the AE recorded during the compression of Vycor samples at two different rates, 1.6 kPa/s (above) and 0.2 kPa/s (below). White lines correspond to the exponent contour levels with a separation of 0.1. The region above the black line indicates an estimated error bar greater than ± 0.05 .

B. Structural transition in FePd

In this second case we present an analysis of the AE recorded during a martensitic transition in Fe-Pd [9]. This alloy has received a lot of theoretical interest due to the simple symmetry relation between the high-temperature phase (cubic) and the low-temperature phase (tetragonal). The transition can be induced by applying an external stress or by changing temperature. Two samples were considered in the study: a single crystal and a polycrystal with the same composition $\text{Fe}_{68.8}\text{Pd}_{31.2}$. The transition was induced by changing the temperature at different driving rates between 0.1 and 10 K/min. Apart from the critical distribution of energies during the events, the AE study revealed other interesting features (which were not found by other techniques). The transition, on cooling, started at the same temperature $M_s = 246 \pm 2\text{K}$ for the two samples. As soon as the transition started, the formation of new tetragonal domains or the advance of interfaces separating previously nucleated domains generated AE events. Due to the thermoelastic behavior [52] of the transition the AE extended for many degrees ($\sim 35\text{K}$) until the sample was fully transformed. On heating, the reverse process occurred with low thermal hysteresis ($\sim 1\text{K}$).

In this case AE was amplified 60 dB and the threshold was chosen to be 22 dB. The four sets of data that we will analyze here correspond to a driving rate of 1 K/min for both the single crystal and the polycrystal and for cooling and heating runs. In order to increase statistics, data were accumulated over 20 ramps. This accumulation technique would correspond to a real increase of the statistics only if the data recorded on each ramp are independent of the previous data. This assumption

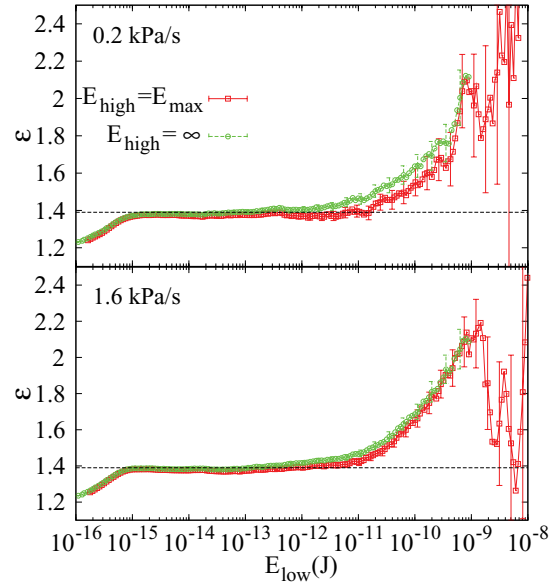


FIG. 6. (Color online) Profiles along the right vertical border of the exponent maps corresponding to the Vycor experiments, compared to the profiles proposed in Ref. [6]. Some typical estimated error bars are shown. The horizontal line indicates the value $\epsilon = 1.39$ proposed in Ref. [8].

is doubtful in the case of structural transitions since it has been demonstrated that samples exhibit a learning process that increases the correlation of the signals between consecutive ramps [53]. In this case the ramps corresponding to the same driving rate were not strictly consecutive since other driving rates were added in between, and thus the independence of the recorded data is not clear.

The total number of recorded signals was $N = 171\,056$ (single crystal, cooling), $N = 111\,840$ (single crystal, heating), $N = 192\,596$ (polycrystal, cooling), and $N = 58\,501$ (polycrystal, heating). Typically, the number of AE events is not symmetric during heating and cooling ramps and there is a lack of understanding of this phenomenon [35].

The study [9] concluded that in the four cases the energies of the individual AE events were power-law distributed (~ 4 decades for the single crystal and ~ 3 decades for the polycrystal). The exponents were fitted using the ML method and were almost independent of the heating or cooling rate. The values of the cutoffs were selected in the region where the statistics were sufficiently high. For the single crystal both cooling and heating ramps exhibited an exponent compatible with a value of 1.64 ± 0.10 . For the polycrystal a clear deviation of the exponent was found between heating (2.0 ± 0.1) and cooling (1.59 ± 0.10). So far, we have no explanation for this deviation.

Figures 7 and 8 show the ML exponent maps corresponding to the four cases. The graphs above correspond to cooling data and the graphs below to heating data. As can be observed the colored spots attached to the diagonal, which correspond to statistical fluctuations, are larger (in absolute terms) than in the previous example. This suggests that, although the recorded number of signals is ~ 10 times larger, most probably data corresponding to the different 20 runs were correlated and did not effectively increase the statistics. Thus, the estimated error

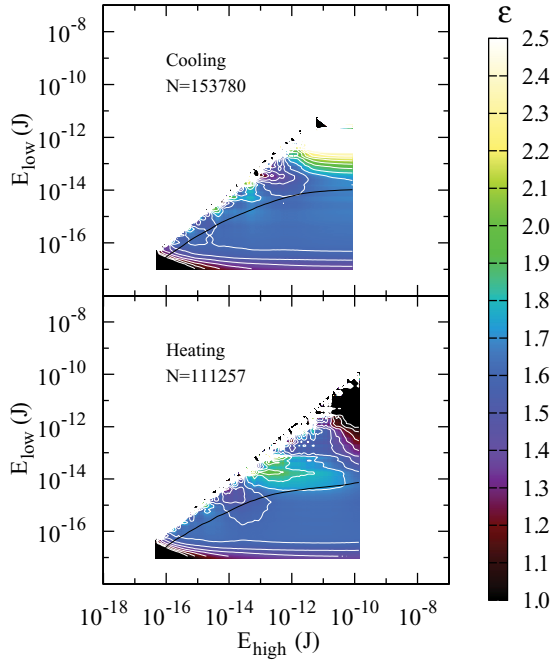


FIG. 7. (Color online) Exponent maps for AE in the FePd single crystal corresponding to heating ramps (below) and cooling ramps (above). The region above the black line corresponds to estimated error bars greater than ± 0.05 , after correcting by a factor of $\sqrt{20}$ due to the possible correlations between measurements (see text). The contour lines (in white) are separated by 0.1 units.

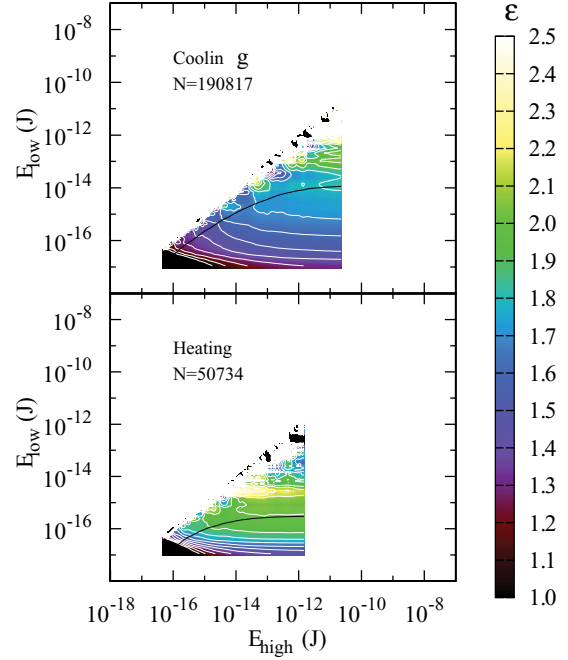


FIG. 8. (Color online) Exponent maps for AE in the FePd polycrystal corresponding to heating ramps (below) and cooling ramps (above). The region above the black line corresponds to estimated error bars above 0.05, after correcting by a factor of $\sqrt{20}$ due to the possible correlations between measurements (see text). The contour lines (in white) are separated by 0.1 units.

bars were, most probably, underestimated by a factor of $\sqrt{20}$. Therefore, in order to plot the curved black line on the map separating the zone with large error bars, we have required that $\sqrt{20}\sigma_{\hat{\gamma}} = 0.05$. It can be seen that, indeed, the curved line separates the zone with fluctuating contour lines from the flat region. By observing the map corresponding to the heating runs (Fig. 8 bottom) for the polycrystalline sample one clearly sees that the large fitted exponent ~ 2.0 is doubtful and most probably is a consequence of the lack of statistics. The region with small enough error bars (below the black line) is very small and it is difficult to identify any plateau. For the cooling ramps (Fig. 8 top) the plateau is not very clear but at least the separation of the contour lines is much wider.

Figure 9 shows the corresponding profiles along the right vertical border of the map. Error bars have been increased by a factor of $\sqrt{20}$ compared to the ones reported in the original paper [9]. The dashed lines indicate the proposed exponent 1.64 ± 0.1 . The hypothesis that this might be a common value for the exponent corresponding to the four cases cannot be ruled out due to the lack of statistics. More measurements for the polycrystalline sample would be required to fully clarify this point.

C. Structural transition in CuZnAl

This third example corresponds to a recent study of AE during the martensitic transition in a CuZnAl shape-memory alloy [10]. In this case the transition is also thermally induced from a monoclinic multivariant structure at low temperatures to a cubic structure at high temperatures. The purpose of

the analysis performed in Ref. [10] was not to demonstrate the power-law distribution of the AE events (which had been shown previously in different studies [54,55]) but to compare the observed exponent with the exponent corresponding to the very large avalanches that can also be recorded by a sophisticated calorimetric study. The sample studied was, therefore, larger than those studied previously. This, as explained above, may lead to distortion of the power law. Furthermore, a larger sample typically requires a more powerful temperature control setup, involving higher electric currents and thus involving greater noise. Since the study was focused on large avalanches and noise was high, the amplification was set to a much lower factor, 40 dB, and the threshold was set to 45 dB. The data set analyzed consists of $N = 17\,936$ signals corresponding to a unique heating ramp.

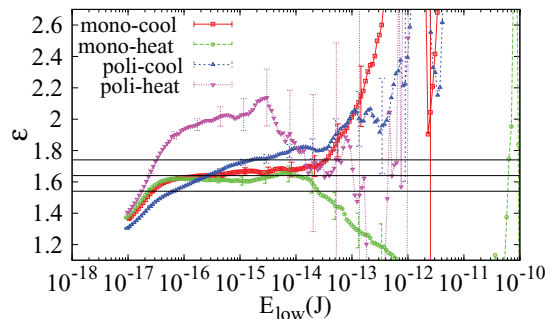


FIG. 9. (Color online) Exponent values vs lower cutoff E_{low} for AE in FePd. The horizontal lines show the value 1.64 ± 0.10 proposed in Ref. [9]

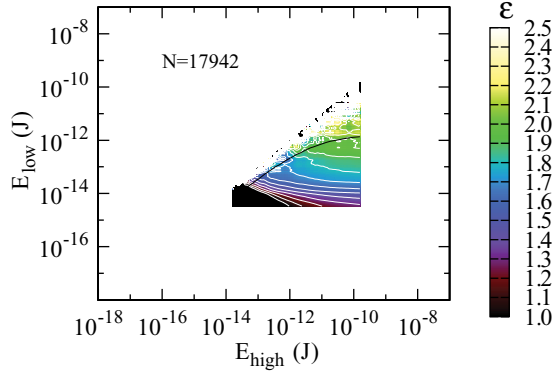


FIG. 10. (Color online) ML exponent map corresponding to the martensitic transition in a CuZnAl sample during a heating ramp.

As can be seen in Fig. 10, the exponent map shows a poorer quality without any clear plateau. The profile shown in Fig. 11, corresponding to the right vertical border of the map, suggests an incipient plateau around $\epsilon = 2$ for slightly more than one decade, but this is not fully conclusive. Thus, the exponent map analysis in this case indicates that either the number of signals is too small to draw conclusions about the power-law behavior of the data or the distribution shows a deformation probably because the sample was too large and attenuation introduces a length scale. Note, however, that we are not fully compromising the results pointed out Ref. [10]. The conclusions were based not only on AE signals but also on the coincidence of the observed incipient plateau at $\epsilon = 2$ with the plateau observed by a different experimental technique.

V. SIMULATION DATA

As a last case we will analyze data corresponding to numerical simulation of a lattice model. This is an interesting illustrative case of the advantages of ML maps compared to the previous proposed analysis assuming no upper limit. This is because the distortions affecting the large avalanche region are not due to measurement problems; rather, they are intrinsic to the finite size of the model. The study corresponds to the 3D Gaussian random field Ising model (3D-GRFIM) driven by an external field $H(t)$ with metastable dynamics at zero temperature [11]. The model is based on the original

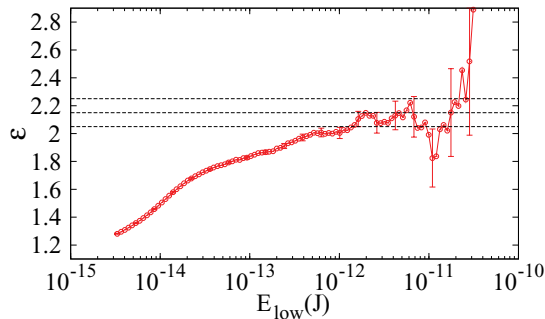


FIG. 11. (Color online) ML fitted exponent as a function of the lower cutoff E_{low} when considering a higher cutoff equal to the maximum recorded signal in the data sample. The horizontal lines indicate the value 2.15 ± 0.10 .

Ising model with the addition of random internal fields h_i acting on each spin $S_i = \pm 1$. The values h_i are quenched and distributed according to a Gaussian probability density $\rho(h) dh = \frac{1}{\sqrt{2\pi}R} e^{-\frac{h^2}{2R^2}} dh$ with zero mean and variance R^2 . The parameter R is usually referred to as the amount of disorder in the system. The Hamiltonian of the system reads

$$\mathcal{H} = - \sum_{\langle i,j \rangle} S_i S_j - \sum_i h_i S_i - H(t) \sum_i S_i, \quad (17)$$

where the S_i spin variables are defined on a regular cubic lattice and the first sum extends over all nearest-neighbor pairs. The simulations of the model start from a saturated configuration $\{S_i\} = -1$ and $H = -\infty$. The field is then adiabatically increased and the spins flip according to the local relaxation rule

$$S_i = \text{sign} \left(\sum_j S_j + h_i + H(t) \right), \quad (18)$$

where the sum extends over all the $z = 6$ neighbors of the spin S_i . With this metastable dynamics the system evolves following a sequence of magnetization jumps (avalanches) occurring at certain fixed values of the external field separated by periods of inactivity in which the field is increased without producing any spin flip.

The model has been widely used as a prototype model for the study of avalanche dynamics. It has been successful in explaining different features of the magnetization process in ferromagnets: the presence of rate-independent hysteresis, the return point memory property, and the existence of Barkhausen noise [11]. Extensions of the model have been also used for the understanding of other athermal first-order phase transitions [56,57].

Here we will focus our attention on the distribution $D(s, R)$ of the sizes s (number of flipped spins) of the avalanches obtained along the magnetization process from $H = -\infty$ to $H = +\infty$, i.e., the so-called integrated distribution. In the thermodynamic limit and when the amount of disorder R is tuned to the critical value R_c , this distribution is expected to be a power law [11,58–60] characterized by a critical exponent called $\tau' = \tau + \sigma\beta\delta$:

$$D(s, R_c) = \frac{s^{-\tau'}}{\sum_{s=1}^{\infty} s^{-\tau'}}. \quad (19)$$

For values of disorder above R_c it is expected that the distribution of avalanche sizes is exponentially damped and thus, in the thermodynamic limit, the discontinuities in the magnetization $\Delta m = s/L^3$ vanish. Below R_c , it is expected that the distribution of avalanches is also exponentially damped, but there will exist a unique massive avalanche with a size proportional to L^3 that is responsible for a magnetization discontinuity, as should occur given the first-order character of the phase transition.

In the numerical simulations on a finite lattice ($L \times L \times L$) with periodic boundary conditions, nevertheless, the distribution of avalanche sizes $D(s, R, L)$ behaves quite differently. Several effects deform the power-law character at the “pseudo”-critical point: On the one hand, avalanche sizes are limited from above by the finite size $s < L^3$. The fact

that, in all critical phenomena with an associated diverging correlation length, distortions occur well below the limit L^3 is well known. Among other reasons, close to the critical point R_c , the avalanches are expected to be fractal [12,60] and thus exceed the lattice side L when its size is much smaller than L^3 . Such avalanches that expand the lattice side L in, at least, one dimension, are the so-called spanning avalanches. For a cubic lattice with periodic boundary conditions, they can be easily classified as 1D-spanning, 2D-spanning, or 3D-spanning depending on whether they span the lattice side in one, two, or three spatial dimensions. On the other hand, some small avalanches (sometimes called lattice animals within percolation theory [61]) may occur for probabilistic reasons even very far away from the critical point. For any value of R and H it is possible to compute the probability that two neighboring spins (surrounded by negative spins) flip simultaneously. The same computation can be carried out for the probability of a group of three, four, etc. neighboring spins with a certain topological configuration to flip simultaneously. It is clear that in such a computation the number of configurations in which spin clusters (lattice animals) with a certain size s can be constructed plays a fundamental role. Such a phenomenon has (*a priori*) no connection with the critical point. The total number of such noncritical avalanches is, nevertheless, very large (it increases with L^3) and renders a distribution of small avalanches that has general, fast decreasing behavior with s , but is nonmonotonic. At the critical point this effect overlaps with the proposed power-law distribution and thus shows a deformation in the small-size region of the distribution $D(s; R, L)$, which typically can be observed below $s \sim 10$. Our goal here is to show how these distortions at large and small sizes show up on the ML exponent map.

Before the discussion of our results, it is important to recall that the exact values of R_c and τ' have not been definitely established. The problems arise precisely because it is difficult to deal with spanning avalanches in the simulations on a finite lattice. There have been two main approaches:

(1) Dahmen and co-workers found $R_c = 2.16 \pm 0.03$ and $\tau' = 2.03 \pm 0.03$ by performing a scaling collapse of the avalanche distribution, neglecting the fact that there should be a dependence on L in the distribution. This was first done [58] on very large systems (up to 1000^3) but averages over very few realizations of disorder. The collapses clearly revealed that corrections to scaling were needed. Later [62], similar collapses were done, which included a unique system size of 64^3 . In both cases, the data were restricted to amounts of disorder $2.25 < R < 6.0$ well above R_c . By this method they avoided most spanning avalanches in the simulations but paid the price of working too far from the critical point and so they had to extrapolate the value for the exponent.

(2) Furthermore, there have been studies precisely focused on the behavior of spanning avalanches which analyze how they concentrate close to the critical point [59,60]. Such studies have performed finite-size scaling analysis of the number of spanning avalanches and have obtained a higher value of the critical amount of disorder $R_c = 2.21$. To do so, the authors proposed a method (called method-2 in Ref. [60]) to separate the 3D-spanning avalanches that will correspond to the massive avalanches that clearly disturb the power-law distribution of avalanche sizes in the region of large events,

close to the critical point. Such 3D-spanning avalanches are identified when they are the unique spanning avalanches in the full-field excursion. This allows them to be filtered from the statistical analysis. The reason behind the separation method is that, when massive avalanches occur, they fill such a large fraction of the system that they do not allow for any other spanning avalanche to take place. It was shown that this filtering method, although not perfect, gave more consistent results in the finite-size scaling analysis than the method of discarding all the spanning avalanches.

The differences between the two above approaches are even more subtle and difficult to summarize here. Let us simply remark that the two analysis use a slightly different scaling variable to measure the distance to the critical point and that the exponent $\tau' = 2.03 \pm 0.03$ proposed in Ref. [58] is interpreted not as a true critical exponent but as an effective exponent τ'_{eff} in Ref. [59]. Instead, the authors of Ref. [59] propose that close to the critical point the distribution of avalanche sizes (neglecting the massive avalanches) will be dominated by noncritical lattice animals (in the small- s region) and by the so-called nonspanning critical avalanches (in the intermediate- and large- s regions). Only the last kind of avalanches may exhibit true power-law behavior with an exponent $\tau_{\text{nsc}} = 1.65$ at $R_c = 2.21$.

We have performed numerical simulations with system sizes ranging from $L = 32$ to $L = 256$ and values of R within the range $2.15 < R < 2.24$. For every size L and every R , averages were taken over 2000 configurations of the random fields for $L \leq 128$ and over 1400 for $L = 256$. We used the RANECU random number generator and a Box-Muller-polar-Marsaglia algorithm to generate the Gaussian random fields. Simulations of the metastable dynamics were done with the sorted list algorithm [63]. The typical sizes of the sample sets of recorded avalanches (corresponding to each single value of R) range from 10^6 for $L = 32$ to 10^9 for $L = 256$.

Figure 12 shows the exponent maps corresponding to $R = 2.20$ and increasing values of L . The first column corresponds to the exponent obtained by considering all the avalanches and the second column to the analysis after the suppression of the massive avalanches, as explained in Ref. [60]. As can be observed in the first column the maps display an approximately triangular black region in the upper right-hand corner that also extends along the right edge which is due to including of such “massive” avalanches that they strongly distort the possible power-law distribution. Massive avalanches overpopulate the large- s region and thus decrease the value of the fitted exponent. Such a deformation disappears when the data are filtered, as can be seen in the right column in Fig. 12.

Close to the bottom horizontal boundary of the maps, exponent oscillations (seen as a sequence of parallel horizontal contour lines) can also be observed in all the graphs. These oscillations are due to noncritical avalanches (lattice animals), which are always present and difficult to subtract.

Besides these two observed deformation regions, it is not clear that a clean plateau exists close to the bottom right-hand corner, with an area increasing with L . The maps show a slow decrease of the exponent from 2.1 toward 1.7 when increasing the lower cutoff s_{low} , and this effect does not seem to disappear for large system sizes. Instead, a region with a value of the exponent close to 1.6–1.7 seems to develop close to the upper

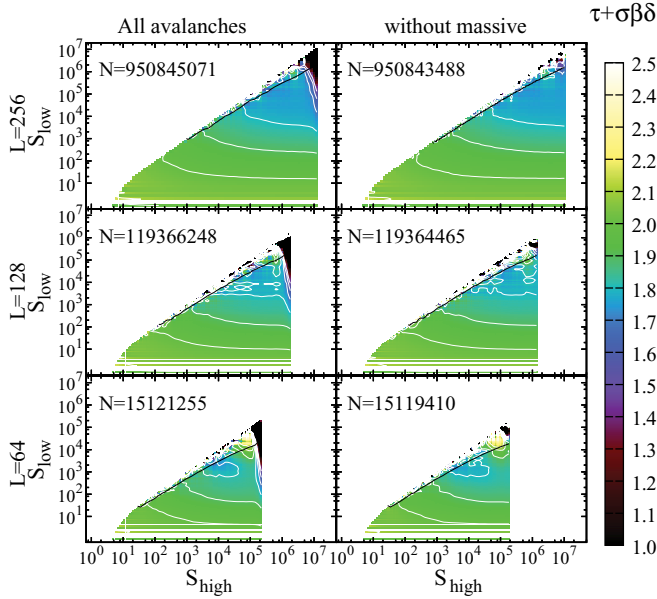


FIG. 12. (Color online) ML exponent maps corresponding to the 3D-GRFIM for $R = 2.20$ and increasing system sizes from $L = 64$ (below) to $L = 256$ above. The left-hand column shows the maps that were obtained by considering all the recorded avalanches, whereas in the right-hand column the method proposed in Ref. [60] was used to suppress the massive, large noncritical avalanches. The region above the black line (very close to the diagonal of the map) corresponds to an estimated error bar of ± 0.05 . Contour lines in white are separated by 0.1 units

corner when the system size is increased up to $L = 256$. This effect is clearer when the data have been filtered (right column) and suggests that a true power law may only be observed when small avalanches are not included in the analysis.

Figure 13 shows the profiles of the maps obtained by fixing $s_{\text{high}} = s_{\text{max}}$, for different values of R between 2.16 and 2.25 and L from 32 to 256. The column on the left corresponds to the analysis of all the avalanches and the column on the right to the analysis after filtering the massive avalanches. Again, it is difficult to find any clear evidence of a plateau growing with L . The only exception seems to be for $R = 2.20$ – 2.21 in the region of intermediate and large cutoffs ($10^4 < s_{\text{low}} < 10^6$), where a plateau seems to form and become broader when L increases. This plateau has a height approaching $\tau' \simeq 1.7$. It can be observed not only on the filtered data (right column) but also as an inflection when the avalanches are not filtered (left column).

The profiles in Fig. 13 also allow the oscillations in the small avalanche region ($s_{\text{low}} < 20$) to be observed. The peaks in the exponent correspond to even sizes. This indicates that small avalanches with odd sizes occur with a higher frequency than the frequency corresponding to a perfect power law.

Note also that, for the critical value $R_c = 2.16$ proposed in Ref. [58], the possible plateau at a height $\tau' \sim 2.03$ does not exhibit a clear tendency to increase with L : it is very much distorted by odd-even fluctuations and, already for $s_{\text{low}} = 10^2$, has clearly decreased for all the studied system sizes.

In our opinion, a final understanding of the behavior of these distributions can only be achieved after a full finite-size

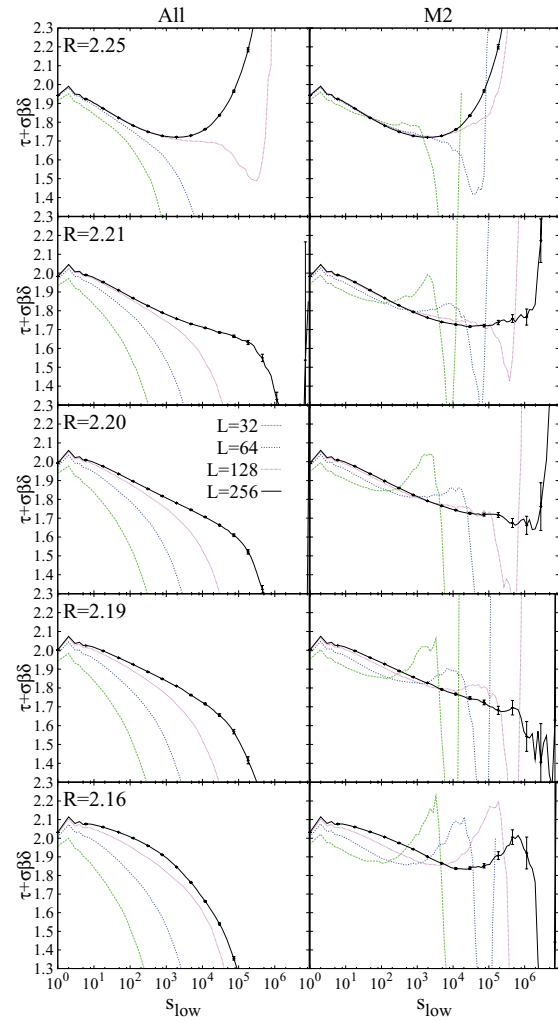


FIG. 13. (Color online) Profiles of the ML exponent maps along the vertical right border for different values of R and L . Data in the left column correspond to the full set of avalanches. On the right column the data correspond to the same sets after filtering the massive avalanches following the method proposed in Ref. [60].

scaling analysis of the distribution $D(s; R, L)$ (involving the three variables), which is beyond the scope of this paper. Nevertheless, in view of the above observations it seems that the distribution of avalanche sizes at the critical point shows two contributions: (i) the actual power-law behavior corresponding to the nonspanning critical avalanches with $\tau' \simeq 1.7$ that can only be observed at intermediate and large avalanche sizes and (ii) the contribution from noncritical avalanches (lattice animals), in the small- s region, which distorts the exponent toward the effective value $\tau'_{\text{eff}} \simeq 2.03$. This scenario is not incompatible with previous numerical studies.

VI. SUMMARY AND CONCLUSIONS

The aim of this paper has been to illustrate the usefulness of ML exponent maps in order to study distortions of power-law behavior to the critical distributions of events. Such distortions are expected to occur for most experimental and numerical simulation data for different reasons. Figure 14 shows a schematic representation of the main conclusions of this paper.

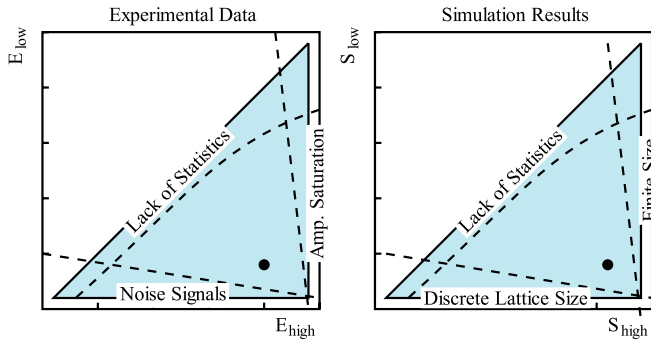


FIG. 14. (Color online) Schematic representation of ML exponent maps for experimental data (left) and simulation data (right). The lines indicate the regions where we can expect deformations of the theoretical plateau. The dot indicates the best values of the cutoffs for the estimation of the exponent.

On the left we show the ML exponent map that one can expect for experimental data. When the sample set is small, a lack of statistics creates deformations of the theoretical plateau close to the diagonal axis of the map, which can be bounded by a proper estimation of the statistical error bars. Noise and undercounting of small-size events renders a deformation region starting in the bottom left-hand corner and which extends horizontally along the bottom border. Saturation of the amplifiers and counters also deforms the plateau in the upper right-hand corner and along the right edge. Between these three boundaries there should be a region with a well-defined plateau. The black dot indicates the best values of the high and low cutoffs for the determination of the critical exponent. It

should be mentioned that, if the size of the sample set is too small, such an ideal situation might not be achieved.

The right plot shows a similar scheme for numerical simulations of lattice systems. The deformation regions are similar to the previous ones. Along the bottom edge we find the footprint of the lattice character of the model that deforms the perfect power-law behavior. Along the vertical right edge we find deformations associated with finite-size effects, which in some cases can be partially corrected.

The examples analyzed in this work have included three seismological catalogs corresponding to Japan, the San Andreas fault, and El Hierro volcanic activity, three sets of acoustic emission data corresponding to the fracture of Vycor under compression, a cubic-tetragonal structural transition in FePd, and a cubic-monoclinic structural transition in CuZnAl, and, finally, numerical simulations of the 3D random field Ising model. These three case studies of the maps have allowed the good quality of the data to be checked or a hypothesis for the observed distortions to be proposed. The studies have also been used to suggest improvements to measurements and/or numerical simulations.

ACKNOWLEDGMENTS

The computations presented in this work have been carried out on the IberGRID infrastructure of the Spanish network e-Ciencia. This work has received financial support from the Spanish Ministry of Innovation and Science (Project No. MAT2010-15114). We acknowledge fruitful comments from Antoni Planes and Pol Lloveras.

[1] D. Sornette, *Critical Phenomena in Natural Sciences*, Springer Series in Synergetics (Springer-Verlag, Berlin, 2000).
 [2] J. P. Sethna, K. A. Dahmen, and C. R. Myers, *Nature (London)* **410**, 242 (2001).
 [3] J. J. Binney, N. J. Dowrick, A. J. Fisher, and M. E. J. Newman, *The Theory of Critical Phenomena* (Clarendon, Oxford, UK, 1992).
 [4] M. L. Goldstein, S. A. Morris, and G. G. Yen, *Eur. Phys. J. B* **41**, 255 (2004).
 [5] H. Bauke, *Eur. Phys. J. B* **58**, 167 (2007).
 [6] A. Clauset, C. R. Shalizi, and M. E. J. Newman, *SIAM Rev.* **51**, 661 (2009).
 [7] O. Peters, A. Deluca, A. Corral, J. D. Neelin, and C. E. Holloway, *Journal of Statistical Mechanics: Theory and Experiments* (2010) P11030.
 [8] E. K. H. Salje *et al.*, *Philos. Mag. Lett.* **91**, 554 (2011).
 [9] E. Bonnot, L. Manosa, A. Planes, D. Soto-Parra, E. Vives, B. Ludwig, C. Strothkaemper, T. Fukuda, and T. Kakeshita, *Phys. Rev. B* **78**, 184103 (2008).
 [10] M. C. Gallardo, J. Machado, F. J. Romero, J. del Cerro, E. K. H. Salje, A. Planes, E. Vives, R. Romero, and M. Stipcich, *Phys. Rev. B* **81**, 174102 (2010).
 [11] J. P. Sethna, K. Dahmen, S. Kartha, J. A. Krumhansl, B. W. Roberts, and J. D. Shore, *Phys. Rev. Lett.* **70**, 3347 (1993).
 [12] O. Perkovic, K. Dahmen, and J. P. Sethna, *Phys. Rev. Lett.* **75**, 4528 (1995).
 [13] W. H. Press, S. A. Teukolsky, W. T. Vetterling, and B. P. Flannery, *Numerical Recipes in FORTRAN*, 2nd ed. (Cambridge University Press, Cambridge, UK, 1992).
 [14] K. S. Miller and S. G. Samko, *Integr. Transf. Spec. Funct.* **12**, 389 (2001).
 [15] W. T. Eadie and F. James, *Statistical Methods in Experimental Physics* (North-Holland, Amsterdam, 1971).
 [16] F. James, *Comput. Phys. Commun.* **60**, 329 (1990).
 [17] This precise value has been chosen because the contour lines of the map, in white, are plotted in steps of 0.1.
 [18] B. Gutenberg and C. F. Richter, *Bull. Seismol. Soc. Am.* **34**, 185 (1944).
 [19] T. Utsu, *Int. Geophys. A* **81**, 733 (2002).
 [20] Y. Y. Kagan, *Geophys. J. Int.* **106**, 135 (1991).
 [21] R. Burridge and L. Knopoff, *Bull. Seismol. Soc. Am.* **57**, 341 (1967).
 [22] Z. Olami, H. J. S. Feder, and K. Christensen, *Phys. Rev. Lett.* **68**, 1244 (1992).
 [23] Y. Ben-Zion and J.-P. Ampuero, *Geophys. J. Int.* **178**, 1351 (2009).
 [24] P. Bak, C. Tang, and K. Wiesenfeld, *Phys. Rev. Lett.* **59**, 381 (1987).
 [25] A. Sornette and D. Sornette, *Europhys. Lett.* **9**, 197 (1989).

- [26] I. Main, *R. Geophys.* **34**, 433 (1996).
- [27] E. M. Scordilis, *J. Seismol.* **10**, 225 (2006).
- [28] T. C. Hanks and H. Kanamori, *J. Geophys. Res.* **84 B5**, 2348 (1979).
- [29] [<http://www.ncedc.org/anss/>].
- [30] P. G. Okubo and K. Aki, *J. Geophys. R.* **92**, 345 (1987).
- [31] S. Hainzl, *J. Geodyn.* **35**, 157 (2003).
- [32] [<http://www.ign.es/ign/layoutIn/volcaFormularioCatalogo.do>].
- [33] W. Wu and P. W. Adams, *Phys. Rev. Lett.* **74**, 610 (1995).
- [34] M. P. Lilly, A. H. Wootters, and R. B. Hallock, *Phys. Rev. Lett.* **77**, 4222 (1996).
- [35] E. Vives, J. Ortín, Ll. Mañosa, I. Ràfols, R. Pérez-Magrané, and A. Planes, *Phys. Rev. Lett.* **72**, 1694 (1994).
- [36] M. L. Rosinberg and E. Vives in *Disordered and Strain-Induced Complexity in Functional Materials*, edited by T. Kakeshita, T. Fukuda, A. Saxena, and A. Planes (Springer, New York, 2010), p. 249.
- [37] For a review on avalanche criticality associated with structural transitions see A. Planes, Ll. Mañosa, and E. Vives, *J. Alloys Compounds*, doi:10.1016/j.jallcom.2011.10.082.
- [38] H. Barkhausen, *Physik Z.* **20**, 401 (1919).
- [39] For a review on criticality associated with Barkhausen noise see G. Durin and S. Zapperi, in *The Science of Hysteresis*, edited by G. Bertotti and I. D. Mayergoyz (Academic, Amsterdam, 2006), Vol. II, p. 181.
- [40] J. Rosti, X. Illa, J. Koivisto, and M. J. Alava, *J. Phys. D* **42**, 214013 (2009).
- [41] M. Kardar, *Phys. Rep.* **301**, 85 (1998).
- [42] D. S. Fisher, *Phys. Rep.* **301**, 113 (1998).
- [43] M. Zaiser, *Adv. Phys.* **55**, 185 (2006).
- [44] M. J. Alava, P. Nukala, and S. Zapperi, *Adv. Phys.* **55**, 349 (2006).
- [45] F. J. Pérez-Reche, L. Truskinovsky, and G. Zanzotto, *Phys. Rev. Lett.* **101**, 230601 (2008).
- [46] C. B. Scruby, *J. Phys. E* **20**, 946 (1987).
- [47] See, for instance, *PCI-2 Based AE System User's Manual*, Rev. 2 (Physical Acoustics Corporation, Princeton Junction, NJ, 2004).
- [48] J. Weiss, F. Lahaie, and J. R. Grasso, *J. Geophys. Res.* **105 B1**, 433 (2000).
- [49] E. Vives, D. Soto-Parra, Ll. Mañosa, R. Romero, and A. Planes, *Phys. Rev. B* **84**, 060101(R) (2011).
- [50] R. A. White and K. A. Dahmen, *Phys. Rev. Lett.* **91**, 085702 (2003).
- [51] F. J. Pérez-Reche, B. Tadic, Ll. Mañosa, A. Planes, and E. Vives, *Phys. Rev. Lett.* **93**, 195701 (2004).
- [52] J. Ortín and A. Planes, *Acta Metall.* **37**, 1433 (1989).
- [53] F. J. Pérez-Reche, M. Stipcich, E. Vives, Ll. Mañosa, A. Planes, and M. Morin, *Phys. Rev. B* **69**, 064101 (2004).
- [54] E. Vives, I. Ràfols, Ll. Mañosa, J. Ortín, and A. Planes, *Phys. Rev. B* **52**, 12644 (1995).
- [55] Ll. Carrillo, Ll. Mañosa, J. Ortín, A. Planes, and E. Vives, *Phys. Rev. Lett.* **81**, 1889 (1998).
- [56] E. Vives and A. Planes, *Phys. Rev. B* **63**, 134431 (2001).
- [57] B. Cerruti and E. Vives, *Phys. Rev. B* **77**, 064114 (2008).
- [58] O. Perkovic, K. A. Dahmen, and J. P. Sethna, *Phys. Rev. B* **59**, 6106 (1999).
- [59] F. J. Pérez-Reche and E. Vives, *Phys. Rev. B* **67**, 134421 (2003).
- [60] F. J. Pérez-Reche and E. Vives, *Phys. Rev. B* **70**, 214422 (2004).
- [61] D. Stauffer and A. Aharony, *Introduction to Percolation Theory*, 2nd ed. (Taylor and Francis, London, 1994).
- [62] Y. Liu and K. A. Dahmen, *Phys. Rev. E* **79**, 061124 (2009).
- [63] M. C. Kuntz, O. Perkovic, K. A. Dahmen, B. W. Roberts, and J. P. Sethna, *Comput. Sci. Eng.* **1**, 73 (1999).